

Classification of the Obstructive Sleep Apnea based on X-ray images analysis by Quasi-conformal Geometry

Hei-Long Chan^a, Hoi-Man Yuen^b, Chun-Ting Au^b, Kate Ching-Ching Chan^b,
Albert Martin Li^b, Lok-Ming Lui^{a,*}

^a*Department of Mathematics, The Chinese University of Hong Kong, Hong Kong*

^b*Department of Paediatrics, Prince of Wales Hospital, The Chinese University of Hong Kong, Hong Kong*

Abstract

Craniofacial profile is one of the anatomical causes of obstructive sleep apnea (OSA). By medical research, cephalometry provides information on patients' skeletal structures and soft tissues. In this work, a novel approach to cephalometric analysis using quasi-conformal geometry based local deformation information was proposed for OSA classification. Our study was a retrospective analysis based on 60 case-control pairs with accessible lateral cephalometry and polysomnography (PSG) data. By using the quasi-conformal geometry to study the local deformation around 15 landmark points, and combining the results with three linear distances between landmark points, a total of 1218 information features were obtained per subject. A L^2 norm based classification model was built. Under experiments, our proposed model achieves 92.5% testing accuracy.

Keywords: obstructive sleep apnea, quasi-conformal theory, image analysis, disease classification, machine learning

*Corresponding author.

Email address: lmloi@math.cuhk.edu.hk (Lok-Ming Lui)

1. Introduction

Obstructive sleep apnoea (OSA) is a common sleep disorder with a reported prevalence of 35% in children and is associated with cardiovascular, metabolic and neurocognitive sequelae [1, 2]. Craniofacial anatomy is one of the major contributing factors in OSA [3]. Cephalometry is a relatively inexpensive, fast and readily available method that provides information on an individual's craniofacial skeletal and soft tissue profile. Common craniofacial characteristics of OSA in children include steep mandibular plane, retrusive chin, longer lower anterior face height and smaller nasopharyngeal airway spaces [3]. These features constitute a more restricted upper airway that poses a higher resistance and collapsibility during sleep.

The distance from the mandibular plane to hyoid bone (MP-H) is one of the most significant apnoea hypopnoea index (AHI)-correlated variables [4, 5, 6, 7]. From our previous study [4], MP-H significantly correlated with the presence of OSA, with an odds ratio of 2.4 when adjusted for age, sex and BMI z-score. A significant positive correlation was also observed between MP-H and OSA severity, when comparing non-OSA group, mild and moderate-to-severe OSA groups in children. The possible relationship between lower hyoid position and OSA is theorized that a descended hyoid position is a compensatory strategy to overcome pharyngeal collapse [8]. Another hypothesis is that the lower hyoid position is caused by enlarged tongue which contributes to airway obstruction [9].

Adenoid hypertrophy and posterior upper airway obstruction are intrinsic aetiology of OSA, causing narrowing of the upper airway and hence airflow

restriction during sleep [2]. They can be assessed effectively using lateral cephalogram [10]. Adenoid size measured by adenoidal-nasopharyngeal ratio (ANR) is significantly correlated with the duration of obstructive apneas [11] and AHI ($r=0.307$, $p=0.034$) [5]. The minimal distance between tongue base and the nearest point on the posterior pharyngeal wall, namely the minimal posterior airway space is found to have an inverse correlation with AHI [7].

Traditional cephalometric analysis focuses on linear distances, angles, ratios and area of pre-identified variables [12]. However, previous studies adopted different protocols and included different sets of variables [5, 6, 8, 13, 14], although the landmarks used were mostly consistent across studies. The diagnostic value of traditional analysis remains limited that certain cephalometric predictors in paediatric population were found but have never been used as the core component for an effective OSA prediction model [5, 15, 16]. Therefore, novel approach to improve cephalometric analysis is needed to enhance its diagnostic accuracy.

Quasi-conformal geometry has been proved to be an effective tool in medical analysis [23, 24, 25, 26, 27, 28, 29]. In particular, it can be used in disease diagnosis such as detecting the Alzheimer’s disease [17, 18] by analyzing the conformality distortion on the hippocampus surface. The tool is also proved to be effective in analyzing the tooth surface for subject dating [19] as an application to bio-archaeology. We are therefore motivated to apply the quasi-conformal geometry to develop an OSA classification model.

In this work, a novel approach to cephalometric analysis for OSA classification was developed using local deformation information around manually labelled landmarks on X-ray images. Quasi-conformal geometry is useful in

establishing landmark-based registration [30, 31, 32]. A quasi-conformal geometry based landmark-based registration model is adopted [20]. The landmark- and intensity-based registration process is to find an optimal transformation between corresponding data based on specific matching features. By analysing the data at specific landmarks on the images using the quasi-conformal geometry, references of the control group and patient group can be established. For new subjects, their corresponding deformation can then be analyzed and compared against the two references. The distance of the subject’s feature vector from that of the control group template and the patient group template is adopted as a classifier for disease prediction. This semi-supervised classification method aims to predict childhood OSA and potentially improve the efficacy of our current diagnostic strategies. And experiments validate that our proposed framework achieves over 92% classification accuracy.

2. Data

2.1. Subjects

This work was a retrospective study based on 60 OSA case-control pairs who were Chinese children recruited for sleep studies in the Prince of Wales Hospital, with accessible lateral cephalometry and polysomnography (PSG) data. OSA and non-OSA groups were defined by $\text{OAHI} \geq 1$ event/h and $\text{OAHI} < 1$ event/h respectively. Lateral cephalometry was taken on the same day of admission. Patients with surgical treatment for OSA prior to cephalometry and PSG, genetic or syndromal disease, congenital or acquired neuromuscular disease, obesity secondary to an underlying cause, or craniofacial abnormalities were excluded. To study the OSA, 15 craniofacial

landmarks are labelled on each image. The landmarks are adopted from [5] and are listed in table (1). Figure (1) demonstrates the craniofacial landmarks on a reference image.

Landmarks	Definitions
N	Nasion, connecting point of frontal bone and nasal bone
S	Sella, midpoint of sella turcica
Ba	Basion, lowest point of clivus
ANS	Anterior nasal spine
PNS	Posterior nasal spine
A	Deepest point of maxillary dimple
B	Deepest point of mandibular dimple
Gn	Gnathion, the most anterior and inferior point on the mandibular symphysis
Me	Menton, the most inferior point on the mandibular symphysis
Go	Gonion, intersection of inferior margin of mandible and posterior margin of mandibular ramus
Ar	Articulare, intersection of basal margin of occiput and posterior margin of mandibular ramus
H	The most anterior and superior point of hyoid bone
Tant	Tip of tongue
u1	Tip of uvula
Va	Vallecula
Phw	The intersection of posterior pharyngeal wall and horizontal line passing hyoid bone
ph1	Anterior point of a the minimal distance between tongue base and posterior pharyngeal wall
ph2	Posterior point of the minimal distance between tongue base and posterior pharyngeal wall

Table 1: Definition of each craniofacial landmark adopted

2.2. Polysomnography

The nocturnal PSG was performed at the Prince of Wales Hospital. A model SiestaTM ProFusion III PSG monitor (Compumedics Telemed, Ab-

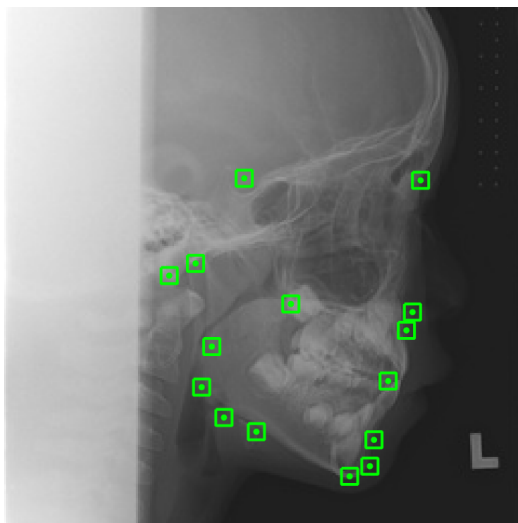


Figure 1: Demonstration of the craniofacial landmark points (green dots) and the surrounding window (green box) superimposed on a sample X-ray input image

botsford, Victoria, Australia) was used to record the following parameters: electroencephalogram (F4/A1, C4/A1, O2/A1), bilateral electrooculogram, electromyogram of mentalis activity and bilateral anterior tibialis. Respiratory movements of the chest and abdomen were measured by inductance plethysmography. Electrocardiogram and heart rate were continuously recorded from two anterior chest leads. Arterial oxyhaemoglobin saturation (SaO₂) was measured by an oximeter with finger probe. Respiratory airflow pressure signal was measured via a nasal catheter placed at the anterior nares and connected to a pressure transducer. An oronasal thermal sensor was also used to detect the absence of airflow. Snoring was measured by a snoring microphone placed near the throat. Body position was monitored via a body position sensor.

An adequate overnight PSG is defined as recorded total sleep time of > 6 hours. Respiratory events including obstructive apnoeas, mixed apnoeas,

central apnoeas and hypopnoeas were scored based on the recommendation from the AASM Manual for the Scoring of Sleep and Associated Events [19]. Respiratory effort-related arousals (RERAs) are scored when there is a fall of $< 50\%$ from baseline in the amplitude of nasal pressure signal with flattening of the nasal pressure waveform, accompanied by snoring, noisy breathing, or evidence of increased effort of breathing. A respiratory event is scored when it lasts ≥ 2 breaths irrespective of its duration. Arousal is defined as an abrupt shift in EEG frequency during sleep, which may include theta, alpha and/or frequencies greater than 16 Hz but not spindles, with 3 to 15 seconds in duration. In REM sleep, arousal is scored only when accompanied by concurrent increases in submental EMG amplitude.

Obstructive apnoea hypopnoea index (OAHl) is defined as the total number of obstructive and mixed apnoeas and hypopnoeas per hour of sleep. Respiratory disturbance index (RDI) is defined as the total number of obstructive and mixed apnoeas, hypopnoeas and RERAs per hour of sleep. Oxygen desaturation index (ODI) is defined as the total number of dips in arterial oxygen saturation $\geq 3\%$ per hour of sleep. Arousal index (ArI) is the total number of arousals per hour of sleep. Respiratory arousal index (RAI) is the total number of arousals per hour of sleep that are associated with apnoea, hypopnoea or flow limitation. Subjects with an OAHl of $< 1/h$ are defined as having no OSA, while those with an OAHl between $1/h$ and $5/h$ and $\geq 5/h$ are defined as having mild and moderate-to-severe OSA respectively. The PSG scoring and reporting was performed by the senior research assistant who has RPSGT qualification and experience in performing paediatric PSG. He/she was blinded to other assessment data of the subjects.

2.3. Lateral X-ray cephalogram

Lateral maxillofacial radiograph was taken on the same day of admission to overnight PSG. All radiographic examination was performed with Direct Digital Radiography System (Carestream DRX-1 Evolution DR System, US) using standardized protocol (70-75kVp, Automatic sensor of around 6-10 mAs, 150-cm film-focus distance).

3. Mathematical Background

In this section, the quasi-conformal theory is reviewed as it is the key concept towards our proposed model. It is the foundation of our registration model and it also contributes to our proposed feature, the conformality distortion, to classify OSA.

3.1. Review on quasi-conformal geometry on 2D domain

Let Ω_1 and Ω_2 be two rectangular image domain, which are regarded as subsets of \mathbb{C} . A diffeomorphism $f : \Omega_1 \rightarrow \Omega_2$ is defined to be conformal if it is a complex function satisfying the Cauchy-Riemann equation

$$\frac{\partial f}{\partial \bar{z}} = 0, \quad (1)$$

where $\frac{\partial}{\partial \bar{z}} = \frac{\partial}{\partial x} + i \frac{\partial}{\partial y}$. A conformal mapping always preserves angles and thus the local geometry is preserved under the mapping.

Then, an orientation-preserving homeomorphism $f : \Omega_1 \rightarrow \Omega_2$ is defined to be quasi-conformal if it satisfies the Beltrami equation

$$\frac{\partial f(z)}{\partial \bar{z}} = \mu(z) \frac{\partial f(z)}{\partial z}, \quad (2)$$

where $\mu : \Omega_1 \rightarrow \mathbb{C}$ is Lebesgue measurable satisfying $\|\mu\|_\infty < 1$, and $\frac{\partial}{\partial z} = \frac{\partial}{\partial x} - i \frac{\partial}{\partial y}$.

Obviously, $\|\mu\|_\infty = 0$ if and only if f is conformal. Hence, the notion of quasi-conformal maps is a generalization of conformal maps. Infinitesimally, suppose $0 \in \Omega_1$, then for any $z \in Nbd(0, \delta)$ where $\delta > 0$ is small, a quasi-conformal mapping f has the following local parametric expression

$$\begin{aligned} f(z) &\approx f(0) + f_z(0)z + f_{\bar{z}}(0)\bar{z} \\ &= f(0) + f_z(0)(z + \mu(0)\bar{z}). \end{aligned} \tag{3}$$

Note that the translation function $f(0)$ and the dilation function $f_z(0)$ are conformal, so all the non-conformality of f is due to the term $D(z) = z + \mu(0)\bar{z}$ which causes f to map an infinitesimal circle to an infinitesimal ellipse (See Figure (2)).

Hence, the study of non-conformality reduces to the analysis of the term μ , which is called the *Beltrami coefficient*. In fact, for any $p \in \Omega$, the angle of maximal magnification is $\arg(\mu(p))/2$ with magnifying factor $1 + |\mu(p)|$ while the angle of maximal contraction is the orthogonal angle $(\arg(\mu(p)) - \pi)/2$ with contraction factor $1 - |\mu(p)|$.

Indeed, by defining μ_f for a complex function f using the equation (2), it can be seen that μ_f can be used to distinguish orientation preserving homeomorphisms.

Theorem 3.1. *Let $f : \mathbb{C} \rightarrow \mathbb{C}$ be a complex mapping. Define*

$$\mu_f = \frac{\partial f}{\partial \bar{z}} \bigg/ \frac{\partial f}{\partial z}, \tag{4}$$

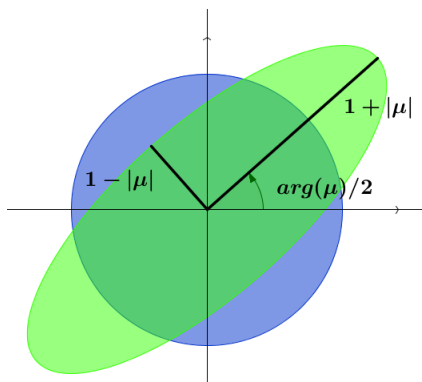


Figure 2: Illustration of the conformality distortion in 2-dimensional space: mapping an infinitesimal disk (blue) to an infinitesimal ellipse (green). The disk and the ellipse are rescaled for illustrative purpose

then $\|\mu_f\|_\infty < 1$ if and only if f is an orientation preserving homeomorphism.

Here, $\mu_f(x)$ is called the conformality distortion of the function f at x . Its magnitude and angle can be used to determine the “distance” of f from being conformal.

Note that there is a one-to-one correspondence between a quasi-conformal mapping f and its Beltrami coefficient μ . Given f , there exists a Beltrami coefficient μ such that (f, μ) satisfies the Beltrami equation. Conversely, the following theorem states that given an admissible Beltrami coefficient μ , there always exists an quasi-conformal mapping f associating to this μ .

Theorem 3.2 (Measurable Riemannian Mapping Theorem). *Suppose $\mu : \mathbb{C} \rightarrow \mathbb{C}$ is Lebesgue measurable satisfying $\|\mu\|_\infty < 1$, then there exists a quasi-conformal homeomorphism f from the unit disk to itself, which is in the Sobolev space $W^{1,2}(\mathbb{C})$ and satisfies the Beltrami equation in the distribution sense. Furthermore, assuming the mapping is stationary at 0, 1 and ∞ , the associated quasi-conformal homeomorphism f is uniquely determined.*

Therefore, under suitable normalization, a homeomorphism from \mathbb{C} to \mathbb{C} can be uniquely determined by its associated Beltrami coefficient. This is a crucial property that allows one to register between two images by homeomorphisms, which can be constructed by applying constraints on the Beltrami coefficient corresponding to the registration mapping.

4. Proposed Model

In this work, we propose to analyze the deformation between X-ray images of skulls to detect OSA. In the first subsection, we discuss the image registration with reference to the craniofacial landmarks. Then, geometric distortions of the deformation are calculated to form a feature vector for each subject, which is the main content of the second subsection. Finally, we develop a classification model using the discriminating feature vectors.

4.1. Image Registration

A landmark-matching registration model is adopted for computing the mutual correspondence between subjects [20]. More specifically, the model develops the registration mapping between images $I_i, I_j : \Omega \rightarrow \mathbb{R}$ of subjects i, j by minimizing the energy

$$E(\mu, f) = \int_{\Omega} |\nabla \mu|^2 + \alpha \int_{\Omega} |\mu|^2 + \beta \int_{\Omega} (I_i - I_j \circ f)^2. \quad (5)$$

The registration mapping is a smooth homeomorphism matching the intensity between I_i, I_j . To incorporate with the landmark constraints, a splitting

variables scheme is used and the corresponding minimization problem is

$$E(\mu, \nu, f) = \int_{\Omega} |\nabla \nu|^2 + \alpha \int_{\Omega} |\nu|^2 + \sigma \int_{\Omega} |\nu - \mu|^2 + \beta \int_{\Omega} (I_i - I_j \circ f^\mu)^2, \quad (6)$$

in which μ is the Beltrami coefficient of f^μ and μ is forced to match with ν by the third term in (6). Using the formulation (6), the landmark constraints can be added to the variational model by constructing a Beltrami coefficient corresponding to a mapping g , which aligns the landmarks exactly and closely resembles μ , in the alternating minimization of (6). This process is done by the Linear Beltrami Solver (LBS). For more details about the formulation of the registration model, readers are referred to [20]. The application of the quasi-conformal registration is beneficial to reduce the calibration error in taking the X-ray photos for each subject. In other words, the effect of global scaling, global rotation and global linear translation are minimized by quasi-conformal mappings.

4.2. Classification Features

Now, suppose we have N subjects in the database, in which the first $N/2$ subjects are in the control class and the last $N/2$ subjects are in the OSA class. As for disease classification, it is common to construct a template subject for the control class. In this work, we propose to construct such template in the space of Beltrami coefficients. In particular, we randomly pick a control subject $I = I_i$ as the reference subject. Each of the images in the database is registered to I by the above registration model. Let f_i be the registration mapping aligning each craniofacial landmark vertex v_k on I to the corresponding vertex v_{ki} on the subject i . For each landmark

point v_k on the template object, a square window centered at v_k of size w is extracted. Thus, each of the 15 windows includes w^2 vertex points. Figure (1) demonstrates the windows at each landmark point. At each vertex point v included, the magnitude $|\mu(v)|$ and the argument $\arg(\mu(v))$ of the Beltrami coefficient μ of f_i is computed. We construct the template deformation to be the mean of the Beltrami coefficient among the control class, that is,

$$\mu_{template}(v) = \frac{\sum_{i=1}^{N/2} \mu(v_i)}{N/2}.$$

To construct features for the classification model, we linearly combine $|\mu|$ and $\arg(\mu)$ at each vertex to describe the local deformation around the vertex. That is, we define the deformation index:

$$E_{deform}^i(v) = \alpha \cdot |\mu_i(v)| + \beta \cdot \frac{\arg(\mu_i(v))}{\pi} \quad (7)$$

for the subject i , where $\alpha, \beta > 0$. Note that since $|\mu(v)| \in [0, 1]$ and $\arg(\mu(v)) \in [0, \pi]$ for every vertex, so a normalization by $1/\pi$ is added to the latter term to balance the contribution of the two measurements towards E_{deform} . The parameters α, β are chosen such that $\alpha^2 + \beta^2 = 1$. The detail of this part will be elaborated in a latter session.

It is noted that among those craniofacial landmarks, some of them (i.e. Phw, ph1, and ph2) which are on the pharyngeal wall cannot be compared directly among subjects. In this work, we incorporate the mutual distances between each pair of them as features for the classification. That is, we include the distance d_i^1 from the mandibular plane to the hyoid bone (MP-H), the distance d_i^2 from the hyoid bone to the posterior pharyngeal wall (H-Phw)

and the lower pharyngeal width d_i^3 (ph1-ph2) in the deformation index.

Incorporating the 3 distance measurements with the deformation index E_{deform} , each subject i is now described by the feature vector

$$C_i = [E_{deform}^i(v_1), E_{deform}^i(v_2), \dots, E_{deform}^i(v_{15 \times w^2}), \bar{d}_i^1, \bar{d}_i^2, \bar{d}_i^3], \quad (8)$$

where \bar{d}_i^j is the normalization of d_i^j across subjects such that $\max(\bar{d}_i^j) = 1$ for all i , for each $j = 1, 2, 3$. In this work, we choose the window size to be $w = 9$, so each subject is represented by $15 \cdot 9^2 = 1215$ deformation index, together with 3 distance measurements. It is noted that if the windows at two different landmark vertices on the same subject overlap with each other, some vertices in the windows will have multiple contribution to C_i .

To further improve the discriminating power of the feature vector, a t-test incorporating the bagging predictors [22] is applied to trim the feature vector (8) with respect to the deformation index. In the traditional t-test, a probability p_k called the p-value is defined and computed for each feature $E_{deform}(v_k)$ which evaluates the discriminating power of the corresponding feature in separating the given two classes. The bagging predictors strategy further improve the stability of the t-test by a leave-one-out scheme. More specifically, a total of N testes are performed. In each test, the i -th subject is excluded temporarily and the t-test is applied on the remaining subjects. This gives the p-value p_k^i for the feature k in the i -th iteration. After all the N testes, the p-value of a feature is computed by

$$p_k = \min_i p_k^i. \quad (9)$$

Finally, the features with low discriminating power can be expelled from our classification machine by choosing only the K features with high discriminating power in order.

Therefore, our model uses the discriminating feature vector

$$\hat{C}_i = [E_{deform}(v_{k_1}), E_{deform}(v_{k_2}), \dots, E_{deform}(v_{k_K}), \bar{d}_i^1, \bar{d}_i^2, \bar{d}_i^3] \quad (10)$$

as the input to our classification machine. Figure (3) illustrates the pipeline generating the discriminating feature vector for each subject from the corresponding deformation mapping to the template subject.

4.3. Classification Machine

Now, we can build the classification model. In this work, we propose to apply a simple L^2 -norm based classification model which is also used in [17]. We first compute the mean of the feature vectors among the NC class:

$$C_{mean} = \text{mean}(\hat{C}_1, \hat{C}_2, \dots, \hat{C}_{N/2}). \quad (11)$$

Then, the L^2 distance between the feature vector of each subject $i = 1, \dots, N$ and the mean feature vector C_{mean} is computed:

$$d_i = \|\hat{C}_i - C_{mean}\|_2. \quad (12)$$

Since we assume that subjects from the control class should possess similar geometry of the skull, the deformation from a control subject i to the chosen template subject I should be small. That is, d_i should be small if $i \leq N/2$. By sorting $\{d_1, d_2, \dots, d_N\}$, there exists an optimal cutting threshold $d_{opt} > 0$

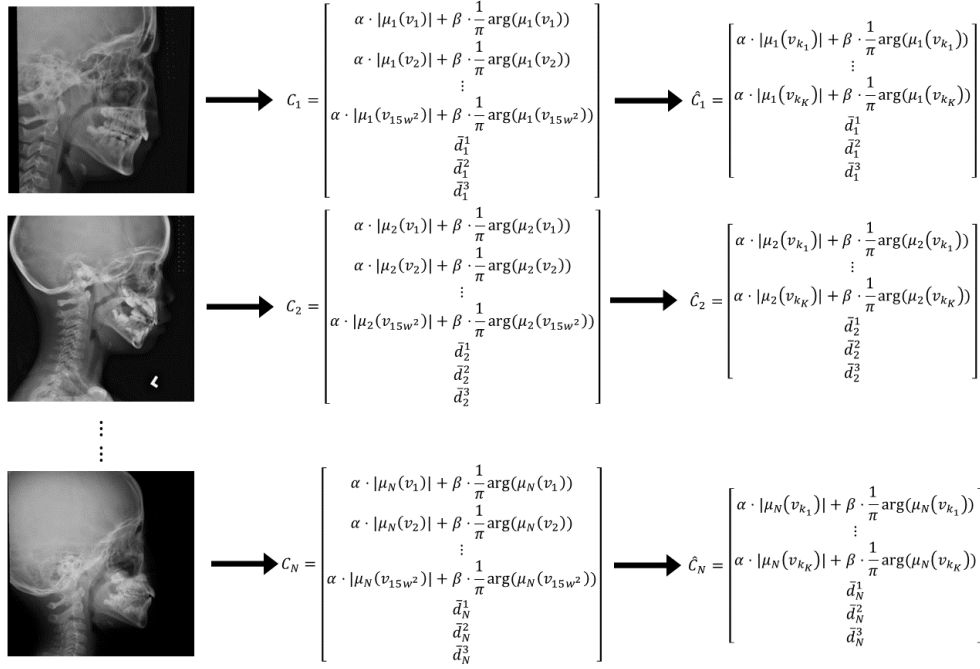


Figure 3: Illustration of the process generating the discriminating feature vector for each subject

maximizing the number of members in the set

$$\left\{i \in \left[1, \frac{N}{2}\right] : d_i < d_{opt}\right\} \cup \left\{i \in \left[\frac{N}{2} + 1, N\right] : d_i > d_{opt}\right\}. \quad (13)$$

That is, d_{opt} is the optimal threshold separating the control class and the OSA class. This gives a classification machine providing an automatic diagnosis for a new subject.

Suppose a new subject is given, to predict if it belongs to the control class or the OSA class, we compute its corresponding feature vector \hat{C}_{new} as in (10)

and hence the distance

$$d_{new} = \|\hat{C}_{new} - C_{mean}\|_2. \quad (14)$$

Then, if $d_{new} < d_{opt}$, we conclude the subject belongs to the control class. Otherwise if $d_{new} > d_{opt}$, we conclude the subjects belongs to the OSA class.

4.4. Parameter Optimization

The parameters α, β in the deformation index (7) can be automatically optimized to maximize the accuracy of the model. It is based on the fact that the discriminating power of the deformation index E_{deform} is invariant under normalization. Therefore, we can constraint the parameter space to lie within the unit circle. In other words, we search for the optimal $(\alpha_{opt}, \beta_{opt})$ in the space

$$\{(\alpha, \beta) \in \mathbb{R}^2 : \alpha > 0, \beta > 0, \alpha^2 + \beta^2 = 1\}. \quad (15)$$

Using the spherical coordinates, we can set a density parameter $\rho \in (0, \frac{1}{2}]$ and compute

$$\alpha_k = \cos k\rho\pi, \quad \beta_k = \sin k\rho\pi, \quad k = 0, 1, \dots, \frac{1}{2\rho}. \quad (16)$$

Each pair of (α_k, β_k) varies the contribution of $|\mu|$ and $\arg(\mu)$ to the deformation index E_{deform} and hence gives a different classification model. The accuracy of each model can then be tested by the 10-fold cross validation and thus the optimal parameter $(\alpha_{opt}, \beta_{opt})$ can be chosen to be the one contributing to the model of the highest validation accuracy. It is noted that the number K in choosing the discriminating features has to be optimized by

hand-tuning.

5. Experiments results

In this work, we are given 120 subjects consisting of 60 control subjects and 60 OSA subjects. To test the accuracy of the proposed model, we perform 100 testes. In each test, we randomly pick 40 control subjects and 40 OSA subjects to compose a sub-database to train the classification model. That is, we apply the 10-fold cross validation onto the sub-database (of size 40) to optimize the parameters (α, β) . In a 10-fold cross validation, the database is partitioned into 10 equal portions and 10 sub-experiments are performed. In each sub-experiment, one portion is excluded and the classification model is built using the remaining data. Afterwards, the subjects in the excluded portion is used to serve as testing subjects. In this manner, each data in the database serve as a testing subject for exactly once and an overall classification accuracy of all the 10 sub-experiments can be calculated. 10-fold cross validation is a very popular validation method to evaluate the accuracy of a classification model if only a small database is given.

For each of the 100 testes, a 10-fold cross validation is performed on the sub-database and the optimal parameters $(\alpha_{opt}, \beta_{opt})$ are obtained. Then, the classification machine is tested with the remaining 20 control subjects and the 20 OSA subjects. This gives a testing accuracy of the proposed machine. The results of the 100 testes are combined to evaluate the mean accuracy of the proposed OSA classification machine.

The highest classification accuracy is 92.5% (sensitivity 95% and specificity 90%) achieved at choosing $K = 500$. That is, 500 vertices out of the 1,218

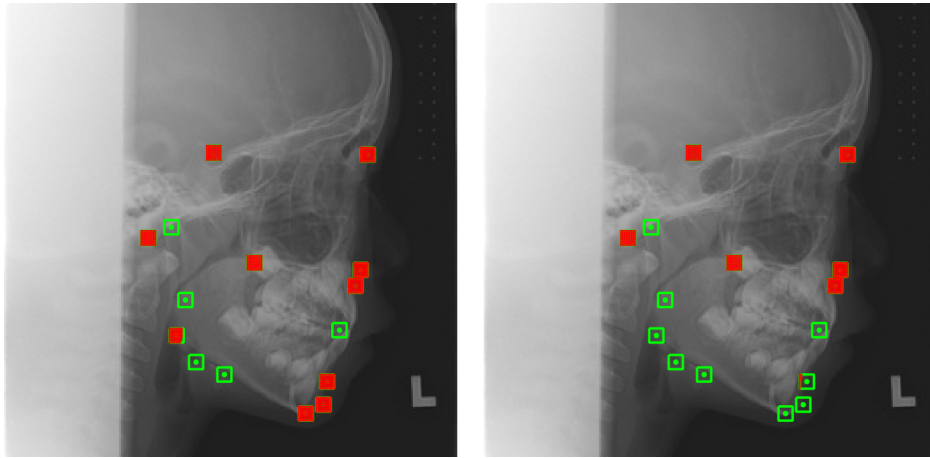


Figure 4: Visualization of the vertices picked (red) by the model in constructing the classification model. (Left) $K = 800$; (Right) $K = 500$.

vertices having the highest discriminating power is chosen. Table (2) records the classification accuracy of the proposed model in choosing different K .

No. of features	$(\alpha_{opt}, \beta_{opt})$	Sensitivity	Specificity	Accuracy
500	(0.985, 0.173)	95.0%	90.0%	92.5%
800	(0.996, 0.089)	89.3%	85.7%	87.5%
1215	(0.989, 0.150)	72.6%	62.6%	67.6%

Table 2: Statistics of the classification accuracy of the proposed model

According to the automatic optimization of the coefficients (α, β) , the magnitude $|\mu|$ of the Beltrami coefficient μ of the deformation has a consistently higher discriminating power over the argument $\arg(\mu)$ of μ in the classification model. This can be explained by the fact that the magnitude $|\mu|$ describes the degree of non-conformal distortion while the argument $\arg(\mu)$ describes the direction of non-conformal distortion.

Figure (4) plots the K vertices with the highest discriminating power. From the figure, it can be seen that some craniofacial landmarks do have

a higher discriminating power to the classification model. This is also a contribution of our model to help validating the discriminating power of each craniofacial landmark in the OSA diagnosis.

5.1. Comparison with other methods

In literature of OSA studies using lateral cephalometry, the majority was comparing the linear distance, angles and ratios measured directly on the cephalogram between the OSA group and control group. To compare our proposed model with the conventional methods, we built another OSA classification machine using the same database.

Twenty-two cephalometric parameters were measured based on the landmarks (listed in table (3) and table (4)). The measurements are stacked to form the feature vector for each subject. Then, we apply the SVM to create the classification model. For fair testing, the 10-fold cross validation is used to test the model with 60 control-OSA pairs of subjects randomly selected from the database. And a total of 100 testes are performed to neutralize possible bias to a certain data separation.

The accuracy of the model using conventional cephalometric parameters is 70.3%. If the top-10 best features among the parameters are extracted (using the bagging-incorporated t-test strategy as in our proposed model), the accuracy is 74.6%. Comparing the accuracy, it is evident that our proposed QC-based model really contributes to a more accurate classification of OSA. This can be explained by the fact that the conformality distortion provides a deeper infinitesimal understanding of the underlying deformation than conventional cephalometric measurements.

6. Conclusion

A new approach to cephalometric analysis using quasi-conformal geometry based local deformation information is proposed for classifying the Obstructive Sleep Apnea (OSA). The proposed model combines information from the conformality distortion with the distance measurements between several craniofacial landmarks to formulate a feature vector to describe each subject. A t-test incorporating the bagging predictor is applied to trim the feature vector and increase its discriminating power. A L^2 -norm based classification machine is built using the trimmed feature vector. Under experiments on a database consisting of 60 OSA case-control pairs, our proposed model achieves 92.5% accuracy in choosing the top 500 best features. In the future, we will apply the current framework in the neural network setting to further improve the accuracy and efficiency.

References

- [1] A. M. Li et al., “Epidemiology of obstructive sleep apnoea syndrome in Chinese children: A two-phase community study,” *Thorax*, vol. 65, no. 11, pp. 991–997, 2010.
- [2] E. Dehlink, “Update on paediatric obstructive sleep apnoea,” *J Thorac Dis*, vol. 8, no. 2, pp. 224–235, 2016.
- [3] P. C. Deegan and W. T. McNicholas, “Pathophysiology of obstructive sleep apnoea,” *Eur. Respir. J.*, vol. 8, no. 7, pp. 1161–1178, 1995.
- [4] C. T. Au, K. C. C. Chan, K. H. Liu, W. C. W. Chu, Y. K. Wing, and A. M. Li, “Potential anatomic markers of obstructive sleep apnea in prepubertal children,” *J. Clin. Sleep Med.*, vol. 14, no. 12, pp. 1979–1986, Dec. 2018.
- [5] R. P.-Y. Chiang, C. M. Lin, N. Powell, Y. C. Chiang, and Y. J. Tsai, “Systematic analysis of cephalometry in obstructive sleep apnea in Asian children,” *Laryngoscope*, vol. 122, no. 8, pp. 1867–1872, Aug. 2012.
- [6] S. Bilici, O. Yigit, O. O. Celebi, A. G. Yasak, and A. H. Yardimci, “Relations between Hyoid-Related Cephalometric Measurements and Severity of Obstructive Sleep Apnea,” *J. Craniofac. Surg.*, vol. 29, no. 5, pp. 1276–1281, Jul. 2018.

- [7] H. Özdemir et al., “Craniofacial differences according to AHI scores of children with obstructive sleep apnoea syndrome: Cephalometric study in 39 patients.”, *Pediatr. Radiol.*, vol. 34, no. 5, pp. 393–399, May 2004.
- [8] E. K. Pae, C. Quas, J. Quas, and N. Garrett, “Can facial type be used to predict changes in hyoid bone position with age? A perspective based on longitudinal data.”, *Am. J. Orthod. Dentofac. Orthop.*, vol. 134, no. 6, pp. 792–797, Dec. 2008.
- [9] T. Iwasaki and Y. Yamasaki, “Relation between maxillofacial form and respiratory disorders in children.”, *Sleep and Biological Rhythms*, vol. 12, no. 1. pp. 2–11, Jan-2014.
- [10] M. P. Major, C. Flores-Mir, and P. W. Major, “Assessment of lateral cephalometric diagnosis of adenoid hypertrophy and posterior upper airway obstruction: A systematic review.”, *American Journal of Orthodontics and Dentofacial Orthopedics*, vol. 130, no. 6. Mosby Inc., pp. 700–708, 2006.
- [11] L. J. Brooks, B. M. Stephens, and A. M. Bacevice, “Adenoid size is related to severity but not the number of episodes of obstructive apnea in children.”, *J. Pediatr.*, vol. 132, no. 4, pp. 682–686, 1998.
- [12] G. T. McIntyre and P. A. Mossey, “Size and shape measurement in contemporary cephalometrics.”, *European Journal of Orthodontics*, vol. 25, no. 3. pp. 231–242, 2003.
- [13] Z. Zhong, Z. Tang, X. Gao, and X. L. Zeng, “A comparison study of upper airway among different skeletal craniofacial patterns in nonsnoring Chinese children.”, *Angle Orthod.*, vol. 80, no. 2, pp. 267–274, Mar. 2010.
- [14] N.; Samman, H.; Mohammadi, and J. Xia, “Cephalometric norms for the upper airway in a healthy Hong Kong Chinese population.”, 2003.
- [15] G. Julià-Serdà et al., “Usefulness of cephalometry in sparing polysomnography of patients with suspected obstructive sleep apnea.”, *Sleep Breath.*, vol. 10, no. 4, pp. 181–187, Dec. 2006.
- [16] P. G. Miles, P. S. Vig, R. J. Weyant, T. D. Forrest, and H. E. Rockette, “Craniofacial structure and obstructive sleep apnea syndrome—a qualitative analysis and meta-analysis of the literature.”, *Am. J. Orthod. Dentofacial Orthop.*, vol. 109, no. 2, pp. 163–172, 1996.
- [17] Chan, Hei Long, Hangfan Li, and Lok Ming Lui. “Quasi-conformal statistical shape analysis of hippocampal surfaces for Alzheimer’s disease analysis.” *Neurocomputing* 175 (2016): 177-187.
- [18] Hei-Long Chan, Anthony, et al. “QC-SPHARM: Quasi-conformal Spherical Harmonics Based Geometric Distortions on Hippocampal Surfaces for Early Detection of the Alzheimer’s Disease.” *arXiv* (2020): arXiv-2003.
- [19] Choi, Gary PT, et al. “Tooth morphometry using quasi-conformal theory.” *Pattern Recognition* 99 (2020): 107064.
- [20] Lam, Ka Chun, and Lok Ming Lui. “Landmark-and intensity-based registration with large deformations via quasi-conformal maps.” *SIAM Journal on Imaging Sciences* 7.4 (2014): 2364-2392.
- [21] Berry, Richard B., et al. “The AASM manual for the scoring of sleep and associated events.” *Rules, Terminology and Technical Specifications*, Darien, Illinois, American Academy of Sleep Medicine 176 (2012): 2012.
- [22] B. Leo, Bagging predictors. *Mach. Learn.* 24 (2) (1996) 123-140.

- [23] Lui, L. M., Lam, K. C., Wong, T. W., Gu, X. (2013). “Texture map and video compression using Beltrami representation.” *SIAM Journal on Imaging Sciences*, 6(4), 1880-1902.
- [24] Lui, L. M., Wong, T. W., Thompson, P., Chan, T., Gu, X., Yau, S. T. (2010, September). “Shape-based diffeomorphic registration on hippocampal surfaces using beltrami holomorphic flow.” In *International Conference on Medical Image Computing and Computer-Assisted Intervention* (pp. 323-330). Springer, Berlin, Heidelberg.
- [25] Zeng, W., Lui, L. M., Gu, X., Yau, S. T. (2008). “Shape analysis by conformal modules.” *Methods and Applications of Analysis*, 15(4), 539-556.
- [26] Lui, L. M., Wong, T. W., Zeng, W., Gu, X., Thompson, P. M., Chan, T. F., Yau, S. T. (2010). “Detection of shape deformities using Yamabe flow and Beltrami coefficients.” *Inverse Problems and Imaging*, 4(2), 311.
- [27] Meng, T. W., Choi, G. P. T., Lui, L. M. (2016). “Tempo: feature-endowed Teichmuller extremal mappings of point clouds.” *SIAM Journal on Imaging Sciences*, 9(4), 1922-1962.
- [28] Lui, L. M., Zeng, W., Yau, S. T., Gu, X. (2013). “Shape analysis of planar multiply-connected objects using conformal welding.” *IEEE transactions on pattern analysis and machine intelligence*, 36(7), 1384-1401.
- [29] Lam, K. C., Gu, X., Lui, L. M. (2015). “Landmark constrained genus-one surface Teichmüller map applied to surface registration in medical imaging.” *Medical image analysis*, 25(1), 45-55.
- [30] Choi, Pui Tung, Ka Chun Lam, and Lok Ming Lui. “FLASH: Fast landmark aligned spherical harmonic parameterization for genus-0 closed brain surfaces.” *SIAM Journal on Imaging Sciences* 8.1 (2015): 67-94.
- [31] Lui, Lok Ming, et al. “Optimization of surface registrations using Beltrami holomorphic flow.” *Journal of scientific computing* 50.3 (2012): 557-585.
- [32] Yung, C. P., Choi, G. P., Chen, K., Lui, L. M. (2018). “Efficient feature-based image registration by mapping sparsified surfaces.” *Journal of Visual Communication and Image Representation*, 55, 561-571.

Categories	Measurements	Definitions
Nasal cavity and nasopharyngea 1 space	Ba-N	The distance from the lowest point of clivus to nasion
	S-N	The distance from sella to nasion
	Ba-S	The distance from the lowest point of clivus to sella
	Ba-S-N	The angle between the lowest point of clivus, sella, and nasion
	Ba-S-PNS	The angle between the lowest point of clivus, sella, and posterior nasal spine
Position of hyoid bone	MP-H	The distance from mandibular plane to hyoid bone
	Gn-Go-H	The angle between the line Gn-Go and the line Go-H
	MP-H/Go-Gn	The position of hyoid bone, the ratio of the distance between mandibular plane and hyoid bone and the length of mandibular body
	H-Phw	The distance between hyoid bone and posterior pharyngeal wall
Soft tissue	ul-PNS	The length of soft palate
	Va-Tant	The length of tongue
	ph1-ph2	The minimal distance between tongue base and posterior pharyngeal wall

Table 3: List of all cephalometric measurements adopted to the conventional classification machine (part A)

Categories	Measurements	Definitions
Maxilla and mandible	Go-Gn	The length of mandibular body
	MP	Mandibular plane, tangent to the lower border of the mandible through menton
	SN-GoGn	The angle between S-N line and Go-Gn line
	PNSANS-GoGn	The angle between maxilla and mandible
	S-N-A	The angle between sella, nasion, and deepest point of maxillary dimple
	S-N-B	The angle between sella, nasion, and deepest point of mandibular dimple
	A-N-B	The angle between the deepest point of maxillary dimple, nasion, and deepest point of mandibular dimple
	Ar-Go-Gn	The angle between the line Ar-Go and the line Go-Gn
	Ar-Go-N	The angle between the line Ar-Go and the line Go-N
N-Go-Gn	The angle between the line N-Go and the line Go-Gn	

Table 4: List of all cephalometric measurements adopted to the conventional classification machine (part B)